Morphological Evolution of $Ba(NO_3)_2$ Supported on α-Al_2O_3(0001): An In Situ TEM Study

C. M. Wang,[†] J. H. Kwak,[‡] D. H. Kim,[‡] J. Szanyi,[‡] R. Sharma,[§] S. Thevuthasan,[†] and C. H. F. Peden[‡]

Environmental Molecular Science Laboratory, Pacific Northwest National Laboratory, P.O. Box 999, Richland, Washington 99352, Institute for Interfacial Catalysis, Pacific Northwest National Laboratory, P.O. Box 999, Richland, Washington 99352, and Center for Solid State Science, Arizona State University, Tempe, Arizona 85287

Received: January 12, 2006; In Final Form: April 24, 2006

A key question for the BaO-based NOx storage/reduction catalyst system is the morphological evolution of the catalyst particles during the uptake and release of NOx. Notably, because the formed product during NOx uptake, $Ba(NO_3)_2$, requires a lattice expansion from BaO, one can anticipate that significant structural rearrangements are possible during the storage/reduction processes. Associated with the small crystallite size of high-surface area γ-Al_2O_3, it is difficult to extract structural and morphological features of $Ba(NO_3)_2$ supported on γ-Al_2O_3 by any direct imaging method, including transmission electron microscopy. In this work, by choosing a model system of $Ba(NO_3)_2$ particles supported on single-crystal α-Al_2O_3, we have investigated the structural and morphological features of $Ba(NO_3)_2$ as well as the formation of BaO from $Ba(NO_3)_2$ during the thermal release of NOx, using ex-situ and in-situ TEM imaging, electron diffraction, energy dispersive spectroscopy (EDS), and Wulff shape construction. We find that $Ba(NO_3)_2$ supported on α-Al_2O_3 possesses a platelet morphology, with the interface and facets being invariably the eight {111} planes. Formation of the platelet structure leads to an enlarged interface area between $Ba(NO_3)_2$ and α-Al_2O_3, indicating that the interfacial energy is lower than the $Ba(NO_3)_2$ surface free energy. In fact, Wulff shape constructions indicate that the interfacial energy is $\sim$1/4 of the {111} surface free energy of $Ba(NO_3)_2$. The orientation relationship between $Ba(NO_3)_2$ and the α-Al_2O_3 is α-Al_2O_3[0001]//$Ba(NO_3)_2$[111] and α-Al_2O_3(1−210)//$Ba(NO_3)_2$(110). Thus, the results clearly demonstrate dramatic morphology changes in these materials during NOx release processes. Such changes are expected to have significant consequences for the operation of the practical NOx storage/reduction catalyst technology.

Introduction

BaO supported on alumina has been extensively studied as a potential storage component of NOx storage/reduction catalysts.[1] The mechanisms associated with the NOx uptake and release by this material have been examined in detail using temperature programmed desorption (TPD), vibrational spectroscopies (e.g., infrared (IR) spectroscopy), X-ray diffraction (XRD), electron microscopy (e.g., transmission electron microscopy (TEM)), and energy dispersive spectroscopy (EDS).[2−13] In previous studies, we investigated the chemical transformations and morphology changes during NOx uptake and release using a combination of experimental capabilities including IR, TPD, TEM, EDS, time-resolved XRD, and ^{15}N solid-state NMR.[12,13] We have proposed that the active NOx adsorption material consists of γ-Al_2O_3 surfaces covered by a monolayer BaO film, and with BaO nanoparticles sitting on top of this film when the BaO loading exceeds that required to form the monolayer coating (e.g., for a 20 wt % BaO/Al_2O_3 sample). When the BaO/Al_2O_3 material is synthesized by the standard "wet-impregnation" method using an aqueous solution containing dissolved $Ba(NO_3)_2$, initially large $Ba(NO_3)_2$ crystallites are formed on the alumina support after drying at low (<473 K) temperatures. A large fraction of the alumina surface remains Ba-free after this procedure. Upon higher temperature ($\sim$773 K) thermal treatment required to prepare the active catalyst, these large $Ba(NO_3)_2$ crystallites decompose to form the nanosized BaO particles and monolayer BaO film. During room-temperature NO_2 uptake, both BaO phases are transformed to a structure now consisting of nanosized (<5 nm) $Ba(NO_3)_2$ particles and a monolayer nitrate phase. Heating the material to higher temperature (573 K) in the presence of NO_2 results in the sintering of the nanosized particles into larger $Ba(NO_3)_2$ crystals (<15 nm). At still higher temperatures, and even in the absence of NO_2, the average particle size of $Ba(NO_3)_2$ crystallites increases further (<32 nm), and then, as $Ba(NO_3)_2$ decomposes between 500 and 900 K, the nanosized BaO particles reform on top of the interfacial BaO monolayer.

While TEM experiments, along with the other techniques, have been instrumental in following these morphology changes, the information content of the experiments has been limited in two important ways. First, as illustrated in Figure 1, it can often be difficult to distinguish the Ba-containing phases from the high-surface area alumina support material, especially when nanosized particles are present. The image of an as-synthesized and dried $Ba(NO_3)_2$/alumina material shows a portion of a large γ-Al_2O_3 grain that is covered by a monolithic cluster of $Ba(NO_3)_2$ grains, identified as such by EDS analysis. In contrast, the rest of the alumina grain appears to be essentially free from $Ba(NO_3)_2$; notably, EDS compositional analysis indicates that this "$Ba(NO_3)_2$ particle free" region results in an atomic ratio of typically Al:Ba = 99:1. Still, the Ba-nitrate particle

* Corresponding author. Tel: (509) 376 4292. Fax: (509) 376 5106. E-mail: chongmin.wang@pnl.gov
[†] Environmental Molecular Science Laboratory, PNNL.
[‡] Institute for Interfacial Catalysis, PNNL.
[§] Arizona State University.

10.1021/jp060235i CCC: $33.50
Published on Web 05/28/2006

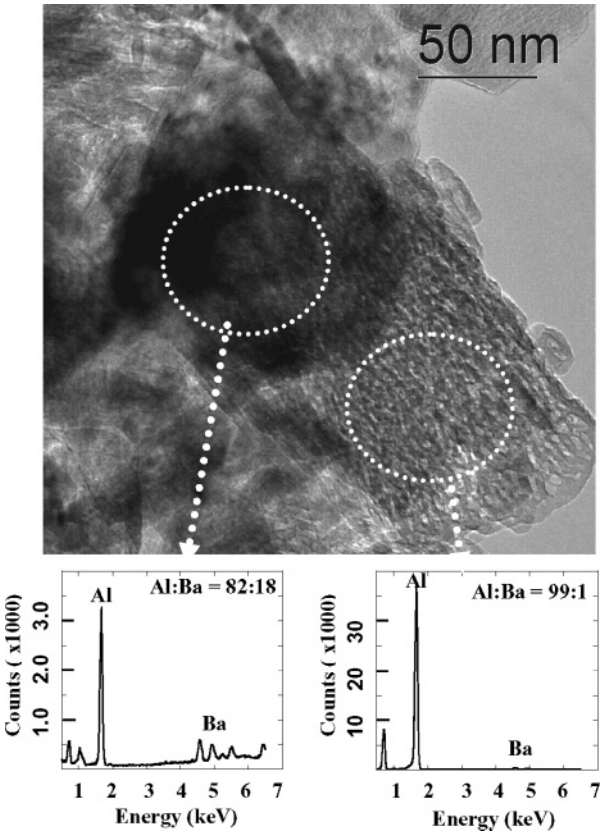

Figure 1. TEM bright-field image of a 20 wt % BaO/γ-Al_2O_3 catalyst prepared by the incipient wetness method using an aqueous $Ba(NO_3)_2$ solution. Note the clustered $Ba(NO_3)_2$ particles on the γ-Al_2O_3 particle near the center of the image. Also included in the figure are EDS spectra from two locations of the sample indicated in the TEM image.

morphologies are generally indistinct and, in particular, the edges of the particles cannot be accurately imaged in this high-surface area material. Thus, for example, no information is available with respect to the relative orientation of $Ba(NO_3)_2$ particles on the γ-Al_2O_3 surface and the influence of these orientations on the morphological transformations. Furthermore, our prior studies on the structural and morphological evolution of alumina-supported Ba-nitrate were mostly examined after the chemical transformations took place. Direct and time-resolved TEM imaging to dynamically monitor the structural and morphological evolution of this material system would be very helpful to better understand the proposed morphology cycles. To address these issues and to understand the effects of crystal orientation, $Ba(NO_3)_2$ was supported on single crystal α-Al_2O_3-(0001) instead of conventional γ-Al_2O_3 powder particles. The structural and morphological evolution of this model system, as a function of calcination temperature, was studied in detail using a combination of ex-situ and in-situ TEM imaging, electron diffraction, EDS, and Wulff shape construction. We recognize some possibly important limitations of the model system used here, including the differences in the extent of surface hydroxylation, and the fact that α-Al_2O_3 contains only octahedral Al atoms while γ-Al_2O_3 contains both octahedral and tetrahedral Al atoms. We plan to address these possible limitations in future studies.

Experimental Section

Electron transparent TEM specimens of single crystal α-Al_2O_3 were prepared by diamond slicing, double-sided dimpling, and finally ion milling with an acceleration voltage of 5 kV for perforation. $Ba(NO_3)_2$ crystallites were loaded on these TEM specimens by putting a drop of aqueous solution of $Ba(NO_3)_2$ on the thin section and leaving the sample to dry at room temperature. The structural and morphological features of the as-prepared α-Al_2O_3-supported $Ba(NO_3)_2$ specimens were characterized using electron diffraction and TEM imaging, carried out with a JEOL JEM 2010 (Tokyo, Japan) microscope using an acceleration voltage of 200 kV and a LaB_6 filament. Response of the $Ba(NO_3)_2$ crystallite to heating was studied in-situ using a 200 kV Tecnai F-20 microscope (FEI, Portland), which is fitted with an environmental cell and field emission electron source. Details of the environmental cell on this microscope have been described elsewhere.[14] For the in-situ TEM experiments, the specimens were heated to 1075 K in a gas mixture of 0.8 N_2 + 0.2 O_2 with a total pressure of 1.0 Torr. During the annealing, the morphological evolution of one $Ba(NO_3)_2$ single-crystal particle was continuously recorded on videotape and periodically recorded using a CCD camera.

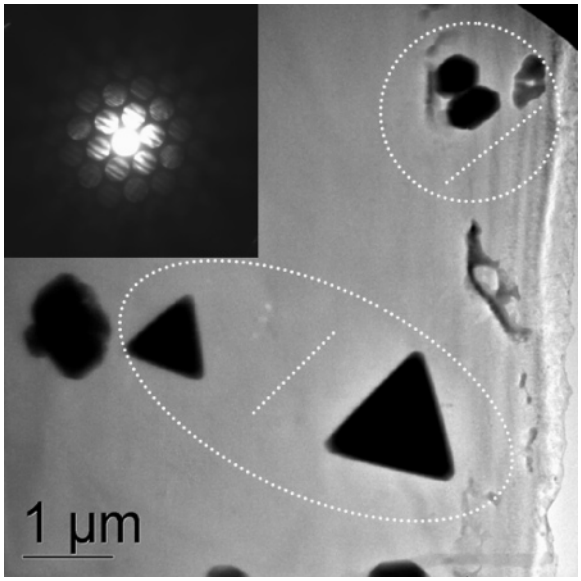

Figure 2. Bright-field TEM image showing the general morphology of the as-prepared $Ba(NO_3)_2$ particles supported on single crystal α-Al_2O_3. Note the aligning of the facet planes of different particles with each other as well as with respect to the underlying support, as indicated by the dashed-line circles and straight lines. The inset is the nanobeam diffraction of the α-Al_2O_3 substrate.

Results and Discussion

The general morphology of $Ba(NO_3)_2$ supported on the single-crystal α-Al_2O_3 is shown in Figure 2. $Ba(NO_3)_2$ possesses a well-defined morphology when imaged in TEM with the substrate oriented along the [0001] zone axis as indicated by the nanobeam electron diffraction pattern. Within the view of Figure 2, the as-prepared $Ba(NO_3)_2$ particles show triangle and polygon morphologies. The facet planes in these triangle and polygon particles appear to be aligned as marked by the dashed line in Figure 2. The alignment of the facet planes indicates that there exists a specific crystallographic orientational relationship among these $Ba(NO_3)_2$ particles themselves, as well as the particles with respect to the α-Al_2O_3 support. Selected area electron diffraction, as shown in Figure 3, indicates that these triangle and polygon shaped $Ba(NO_3)_2$ particles are all single crystals. Based on these electron diffraction results, the crystallographic orientation relationship can be written as α-Al_2O_3-[0001]//$Ba(NO_3)_2$[111] and α-$Al_2O_3(1\bar{2}10)$//$Ba(NO_3)_2$ (110).

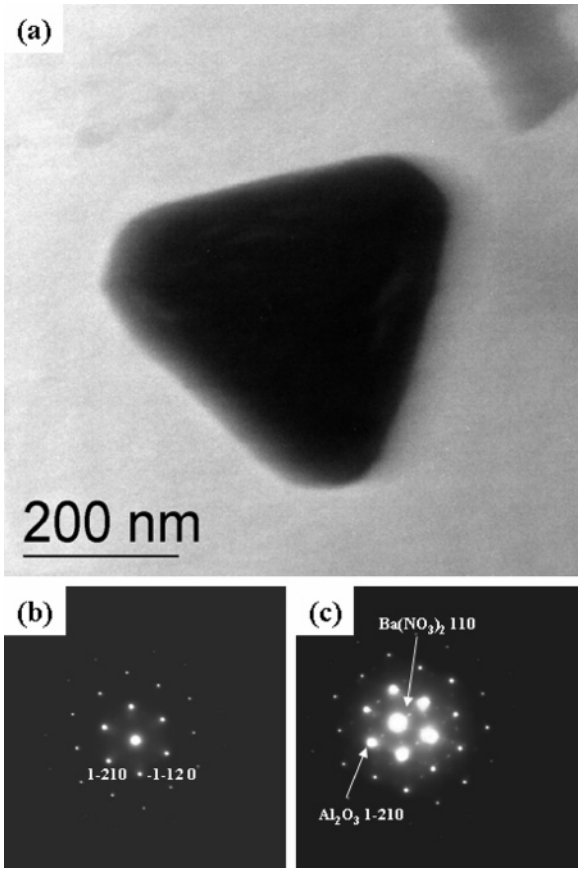

Figure 3. (a) Truncated triangular-shaped $Ba(NO_3)_2$ particle supported on single crystal α-Al_2O_3, (b) electron diffraction from the substrate, and (c) electron diffraction from both the substrate and the $Ba(NO_3)_2$ particle. Note the orientational relationships observed are α-Al_2O_3-[0001]//$Ba(NO_3)_2$[111] and α-Al_2O_3(1−210)//$Ba(NO_3)_2$(110).

Three-dimensional morphologies of the $Ba(NO_3)_2$ particles can be extracted using Wulff shape construction. For a specific crystal symmetry system in a free growth environment, the crystal shape depends on the growth rate of the crystal along different growth directions. For a specific crystallographic direction, the growth rate is proportional to the surface energy of the lattice plane that is perpendicular to the growth direction. For a cubic structure, if all of the equivalent lattice planes grow freely, a range of morphological structures can be generated depending on the growth rate of one group of lattice planes relative to other groups. Figure 4 shows three typical morphologies of cubic structure crystals with the facets defined by two groups of lattice planes: {001} and {111}. The crystal morphology is determined by the ratio of the growth rate along the ⟨001⟩ to that along the ⟨111⟩ directions, which is commonly denoted as R. For example, $R = 0.58$ gives a cubic morphology with the facets being defined by six {001} planes. For the case of $R = 1.0$, a truncated octahedron with six {001} and eight {111} type of facet planes is obtained, while an $R = 1.73$ value yields an octahedron structure with eight {111} plane facets. A detailed description of the morphology with other values of R has been discussed by Wang.[15]

When a $Ba(NO_3)_2$ particle nucleates and grows on the α-Al_2O_3 support, the $Ba(NO_3)_2$/α-Al_2O_3 interface energy is different from the $Ba(NO_3)_2$ surface free energy. Therefore, the growth rate along the direction that is perpendicular to the interface will be different from other crystallographic directions. From the point of view of thermodynamics, the crystal will adopt a morphology such that the surface and interface free energies are minimized. Figure 5 shows the observed morphologies of the as-prepared $Ba(NO_3)_2$ particles along with their Wulff shape constructions. Based on these Wulff shape constructions, it is clear that the $Ba(NO_3)_2$ particles supported on a single crystal α-Al_2O_3 adopt a platelet morphology, with the surfaces and interfaces being invariably defined by eight {111} type planes. These observations are consistent with the general expectation based on the following physical principle. As indicated in Table 1, for cubic structured $Ba(NO_3)_2$, the {111} type plane is the closest packed plane. Therefore, the {111} planes correspond to the lowest free energy surfaces. Formation of platelet morphology for $Ba(NO_3)_2$ on α-Al_2O_3 indicates that the interfacial energy between $Ba(NO_3)_2$/α-Al_2O_3 is lower than the {111} surface free energy, leading to the general tendency to enlarge the interface for minimization of the total free energy of the system. Equivalence of the eight {111} planes means that the $Ba(NO_3)_2$ particles are free to adopt a range of morphologies such as triangles and truncated triangles, as shown in Figure 5. Based on the Wullf shape constructions, we find that the thickness of the platelet is approximately 1/4 of the lateral dimensions. This slower growth rate perpendicular to the Ba-nitrate/alumina interface indicates that the interfacial free energy between $Ba(NO_3)_2$ and α-Al_2O_3 is approximately 1/4 of the {111} surface free energy of $Ba(NO_3)_2$.

Decomposition of the single-crystal $Ba(NO_3)_2$ particles supported on α-Al_2O_3 was monitored in real-time during the annealing of the specimen in an environmental TEM with a gas mixture of 0.8 N_2 + 0.2 O_2 at a total pressure of 1 Torr. During the high-temperature annealing up to 1075 K, the $Ba(NO_3)_2$ decomposed to form BaO. Following the decomposition, two significant changes were observed in the $Ba(NO_3)_2$ particles as illustrated in the TEM images in Figure 6 and Figure 7. (1) The resultant BaO particle still retains a similar overall morphology as its parental single-crystal $Ba(NO_3)_2$ particle. The particle appears to go through a uniform shrinkage, therefore,

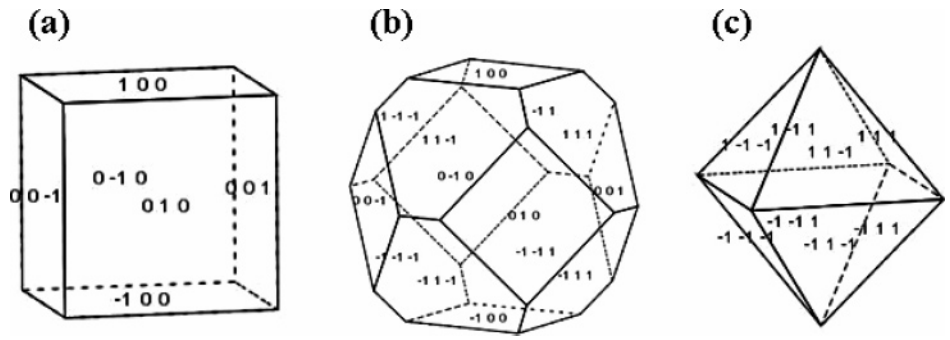

Figure 4. Dependence of particle morphologies on the ratio, R, of the growth rate along the ⟨100⟩ direction to that of the ⟨111⟩ direction for a cubic structure. (a) $R = 0.58$ leads to six {100} planes defining a cube, (b) $R = 1.0$ leads to six {100} planes and eight {111} planes defining a truncated octahedron, and (c) $R = 1.73$ leads to eight {111} planes defining an octahedron.

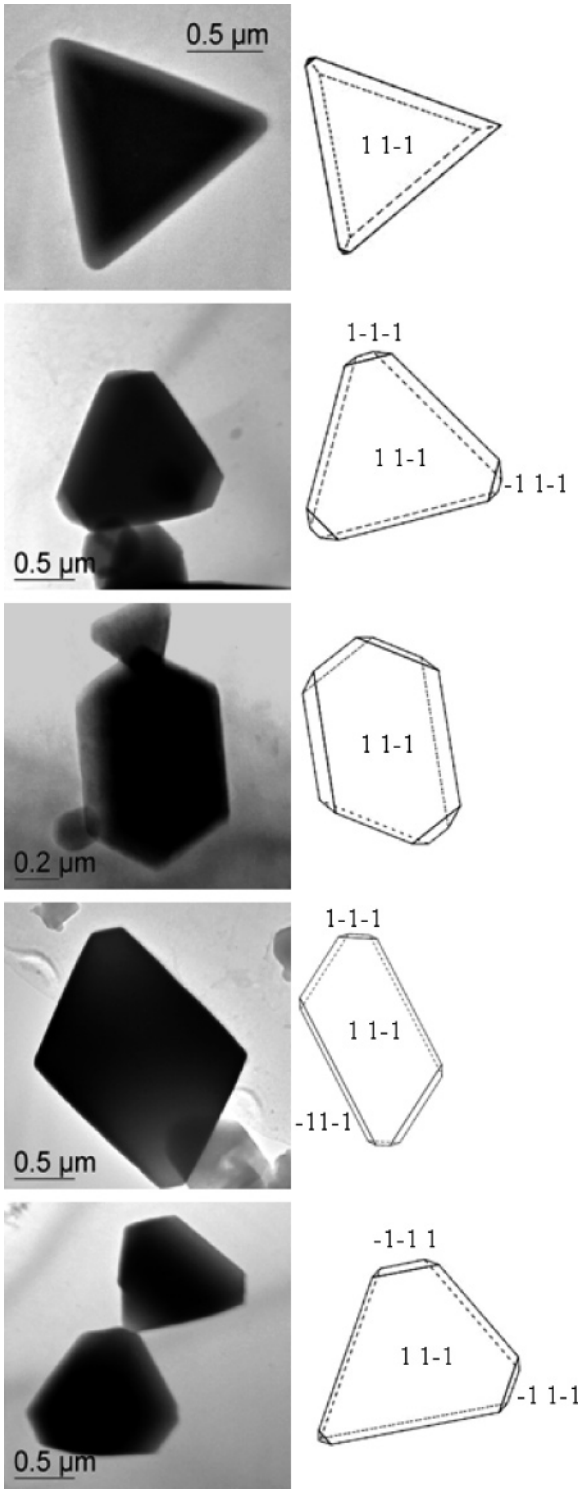

Figure 5. Platelet morphological structures of $Ba(NO_3)_2$ supported on α-Al_2O_3 along with their Wulff shape construction. All of the platelets are defined by eight {111} planes.

TABLE 1: Crystal Structure Data of $Ba(NO_3)_2$, BaO, and α-Al_2O_3

	structure	space group	lattice constant/nm
$Ba(NO_3)_2$	cubic	$P2_13$	$a = 0.8118$
BaO	cubic	Fm-3m	$a = 0.5539$
α-Al_2O_3	trigonal	*R*-3c	$a = 0.4758$, $c = 1.2991$

maintaining its original morphological shape. (Note that the image in Figure 6a was taken in a high-vacuum microscope and Figure 6b was taken in the environmental microscope

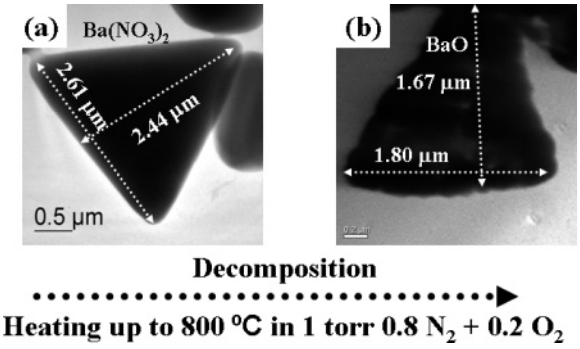

Figure 6. Morphological evolution of a triangular-shaped $Ba(NO_3)_2$ particle supported on single crystal α-Al_2O_3, during in-situ annealing in an environmental TEM: (a) as-prepared, (b) after annealing to 1075 K in 0.8 N_2+ 0.2 O_2 with a total pressure of 1 Torr. Note the linear shrinkage of ~31%, which is comparable with the theoretical value of 32%.

following the decomposition. This accounts for the relative orientation of the images.) The measured linear shrinkage of the particle following the decomposition is ~31%, which approximately equals the theoretically expected linear shrinkage of 32%, assuming that the newly formed BaO particles are single crystals or a fully dense polycrystalline compact. (2) The large particle divided into small crystalline BaO particles as can be discerned from a careful visual analysis of Figure 6b. These fine structural features are further illustrated by the bright-field TEM images and selected area electron diffraction patterns shown in Figure 7, obtained following the annealing of $Ba(NO_3)_2$ at 775 K for 2 h in He. Figure 7 indicates that the BaO particles are not single crystals, instead being a collection of clusters of relatively small BaO particles. Furthermore, detailed electron diffraction analysis indicates that these BaO particles show neither orientational correlation among themselves nor specific orientational relationships with respect to the α-Al_2O_3 substrate. This is demonstrated by the random orientation of the diffraction spots contributed by the BaO particles as shown in Figure 7b and 7d. In these patterns, the diffraction spots related to the BaO particles can be identified by the superimposed computer simulated electron diffraction ring pattern of BaO. There are a number of possible ways to account for the observed random orientations of multiple BaO particles that derive from a single single-crystal $Ba(NO_3)_2$ particle. With regard to lattice plane mismatch, one might argue that BaO would be more favorable than $Ba(NO_3)_2$ for a specific orientation; i.e., BaO(200) − 0.2770 nm, $Ba(NO_3)_2$(220) − 0.2870 nm, and α-Al_2O_3(11−20) − 0.2379 nm. Although the actual interface structure has not been observed in our experiments to date, this simple comparison is counter to the present observations. At least a couple of additional factors may be considered as possible ways to account for the nonuniform orientation of the BaO particles. First, we note that the uneven surface structure of the thin foil α-Al_2O_3 prepared by ion-milling (the TEM specimen), normally giving a wedge-shaped thin section, may sufficiently alter the alumina surface structure to affect the just-described differences in lattice mismatch. Furthermore, the mechanism for the formation of the small crystalline BaO particles through the high-temperature decomposition of $Ba(NO_3)_2$ is not clear; for example, whether it is a process of formation of amorphous BaO followed by nucleation and growth of crystalline BaO or a direct formation of the BaO lattice through a reconstruction of the parental $Ba(NO_3)_2$ lattice following the release of NOx species. Finally, we note that some diffraction spots in the patterns of Figure 7 do not belong to either the α-Al_2O_3 substrate or the BaO particles. One of the

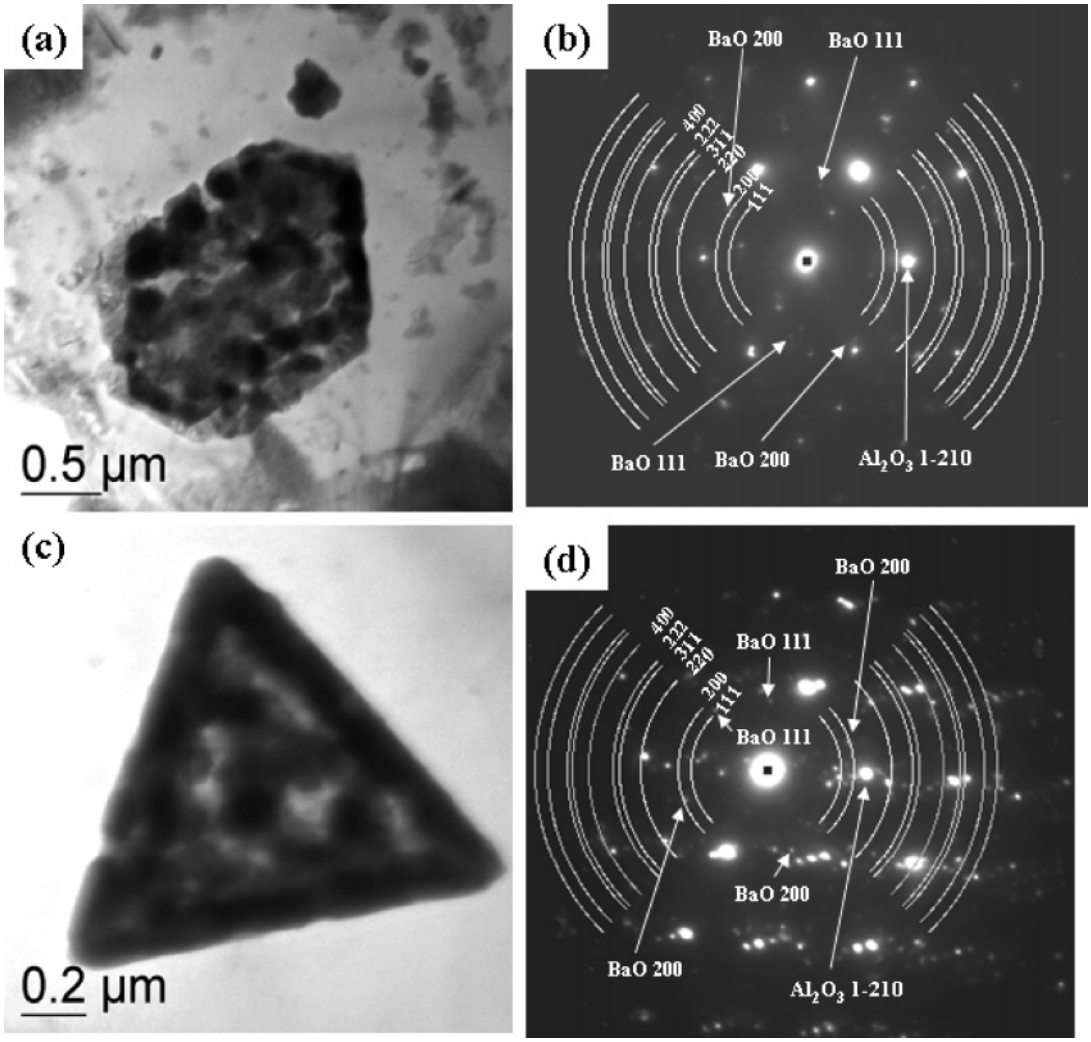

Figure 7. Morphology of BaO particles following the decomposition of $Ba(NO_3)_2$. The BaO particles collectively show the parental morphology of the $Ba(NO_3)_2$. The right side of the figure (b and d) provide the selected area electron diffraction patterns. The computer simulated electron diffraction ring pattern of BaO is superimposed on the experimental pattern to identify the diffraction spots related to the BaO particles.

possible phases related to these additional diffraction spots is $BaAl_2O_4$. However, it is not possible to conclusively determine this phase based on the few extra diffraction spots observed here, which also show no apparent correlation to each other in the diffraction pattern. Thus, further systematic studies are needed to identify additional phases within this system.

The current observations, using direct in-situ imaging methods, followed morphological changes of $Ba(NO_3)_2$ particles supported on α-alumina during their decomposition. An atomic level understanding of the interface between alumina (both γ- and α-phases) and $BaO/Ba(NO_3)_2$ cannot be drawn based solely on the present experimental observations. A proper way to obtain the atomic structural information across the interface between $BaO/Ba(NO_3)_2$ and alumina is to orient the interface such that it is parallel with the electron beam. Such experiments will be difficult, however, due to concerns about the stability of $BaO/Ba(NO_3)_2$ under the irradiation of high energy electron. Instead, we hope to obtain the atomic structural information across the interface by using scanning transmission electron microscopy (STEM) with high-angle-annular-dark-field (HAADF) imaging methods in future studies.

Recognizing the possible limitations of the model system used here with respect to the extent of surface hydroxylation and differing surface structures compared to the real materials, the dramatic changes in morphology observed here during $Ba(NO_3)_2$ decomposition may have important consequences for the operation of the practical NOx storage/reduction catalysts systems. For example, intimate contact between the Ba phase and Pt particles, thought to be important for optimum operation of this technology,[1] may be interrupted during NOx uptake and release. The present studies represent our first attempts to follow these morphology changes at the atomic level. In future work, we plan to specifically address the dependence of the morphology changes on alumina surface structure and extent of hydroxylation.

Conclusions

$Ba(NO_3)_2$ particles supported on single-crystal α-Al_2O_3 possess a platelet morphology, and invariantly faceted in eight {111} lattice planes. Formation of the platelet morphology indicates that the interfacial free energy defined by $Ba(NO_3)_2$ and α-Al_2O_3 is lower than the surface free energy associated with the {111} plane of $Ba(NO_3)_2$. Based on Wulff shape constructions, we find that the interface free energy is approximately 1/4 of the surface free energy associated with the {111} plane of $Ba(NO_3)_2$. The crystallographic orientation relationships between $Ba(NO_3)_2$ and α-Al_2O_3 are determined to be α-Al_2O_3[0001]//$Ba(NO_3)_2$[111] and α-Al_2O_3(1−210)//$Ba(NO_3)_2$(110). Upon high-temperature annealing, the single-crystal $Ba(NO_3)_2$ particles decompose to form multiple BaO

particles, which are clustered together and maintain the overall morphology of the parent $Ba(NO_3)_2$. Thus, the results clearly demonstrate dramatic morphology changes in these materials during NOx release processes. Such changes are expected to have significant consequences for the operation of the practical NOx storage/reduction catalyst technology.

Acknowledgment. This work was supported in part by the Laboratory Directed Research and Development (LDRD) program of Pacific Northwest National Laboratory, and the Office of FreedomCar and Vehicle Technologies, U.S. Department of Energy (DOE). Much of the work was performed in the Environmental Molecular Sciences Laboratory (EMSL) at the Pacific Northwest National Laboratory (PNNL). The EMSL is a national scientific user facility and supported by the U.S. DOE's Office of Biological and Environmental Research. PNNL is a multiprogram national laboratory operated for the U.S. Department of Energy by Battelle Memorial Institute under contract number DE-AC06-76RLO 1830. The use of the John Cowley Center for High Resolution Microscopy is gratefully acknowledged.

References and Notes

(1) Epling, W. S.; Campbell, L. E.; Yezeretz, A.; Currier, N. W.; Parks, J. E., II *Catal. Rev.-Sci. Eng.* **2004**, *46*, 163, and references therein.
(2) Mahzoul, H.; Brilhac, J. F.; Gilot, P. *Appl. Catal., B* **1999**, *20*, 47.
(3) Anderson, J. A.; Paterson, J. A.; Fernandez-Garcia, M. *Stud. Surf. Sci. Catal.* **2000**, *130*, 1331.
(4) Lietti, L.; Forzatti, P.; Nova, I.; Tronconi, E. *J. Catal.* **2001**, *204*, 175.
(5) Prinetto, F.; Ghotti, G.; Nova, I.; Lietti, L.; Tronconi, E.; Forzatti, P. *J. Phys. Chem. B* **2001**, *105*, 12732.
(6) Westerberg, B.; Fridell, E. *J. Mol. Catal A* **2001**, *165*, 249.
(7) Prinetto, F.; Ghiotti, G.; Nova, I.; Lietti, L.; Tronconi, I.; Forzatti, P. *Phys. Chem. Chem. Phys.* **2003**, *5*, 4428.
(8) Su, Y.; Amiridis, M. D. *Catal. Today* **2004**, *96*, 31.
(9) Broqvist, P.; Gronbeck, H.; Fridell, E.; Panas, I. *J. Phys. Chem. B* **2004**, *108*, 3523.
(10) Nova, I.; Castoldi, L.; Lietti, L.; Tronconi, E.; Forzatti, P.; Prinetto, F.; Ghiotti, G. *J. Catal.* **2004**, *222*, 377.
(11) Fanson, P. T.; Horton, M. R.; Delgass, N. W.; Lauterbach, J. *Appl. Catal. B* **2003**, *46*, 393.
(12) Szanyi, J.; Kwak, J. H.; Kim, D. H.; Burton, S. H.; Peden, C. H. F. *J. Phys. Chem. B* **2005**, *109*, 27.
(13) Szanyi, J.; Kwak, J. H.; Hanson, J. C.; Wang, C. M.; Szailer, T.; Peden, C. H. F. *J. Phys. Chem. B* **2005**, *109*, 7339.
(14) Sharma, R. *J. Mater. Res.* **2005**, *20*, 1695.
(15) Wang, Z. L. *Adv. Mater.* **1998**, *10*, 13.